A new global average model of the coupled thermosphere and ionosphere

C. G. Smithtro[1] and J. J. Sojka

Center for Atmospheric and Space Sciences, Utah State University, Logan, Utah, USA

Received 8 September 2004; revised 21 March 2005; accepted 2 June 2005; published 18 August 2005.

[1] A model representing the global average ionosphere and thermosphere (GAIT) is developed as a tool to explore the response of the coupled system to changes in the input solar irradiance between 3 and 360 nm. The GAIT model self-consistently solves the coupled continuity, momentum, and energy equations for the three major neutral species, N_2, O_2, and O, as well as minor neutral constituents important to the global energy budget. In the ionosphere the model includes five different ion species and two excited states of O^+. The GAIT model also includes an approximate treatment of photoelectrons, in order to calculate secondary ionization and thermal electron volume heating rates. After examining the sensitivity of the GAIT model to uncertainties in key reaction rates and inputs, we consider its response to four different extreme ultraviolet irradiance models. With three of the irradiance models we reproduce the expected variation in exospheric temperature to within 2%; however, the dynamic range of the fourth is deemed to be too small. We conclude with an analysis of the model's wavelength-dependent sensitivity to input solar photons.

Citation: Smithtro, C. G., and J. J. Sojka (2005), A new global average model of the coupled thermosphere and ionosphere, *J. Geophys. Res.*, *110*, A08305, doi:10.1029/2004JA010781.

1. Introduction

[2] In a series of papers spanning over 20 years, R. G. Roble and others pioneered the concept of a 1-D global mean model of the upper atmosphere. Their work culminated with the creation of coupled models representing the thermosphere/ionosphere [*Roble et al.*, 1987, hereinafter referred to as R87] and mesosphere/thermosphere/ionosphere [*Roble*, 1995, hereinafter referred to as R95]. These papers showed that a relatively simple 1-D model could be used to accurately represent the global average state of the upper atmosphere over the course of a typical solar cycle.

[3] A global average model obviously neglects horizontal structure and transport; instead, it represents a climatological view of the total system. An appreciation of the model's strengths and weaknesses is therefore crucial. Consider empirical models of the thermosphere and ionosphere; they are useless when it comes to predicting high-resolution variability due to space weather, but ideal for generating climatology at a given location. In the same manner, a global average model cannot answer questions involving horizontal or diurnal structure, but does provide a physically realistic picture of how an idealized atmosphere responds to solar input. Sophisticated 3-D models provide a more complete picture, but are much more complex, have exponentially greater computational requirements, and are more difficult to interpret.

[4] The ultimate goal of this work is to explore the global response of the thermosphere and ionosphere to irradiance inputs outside the range of the normal solar cycle. This will require extrapolations of the solar irradiance to previously unmeasured levels, a speculative proposition. In that light, a full 3-D general circulation models is not warranted, whereas a 1-D global average model is ideally suited to the task.

[5] Borrowing extensively from R87 and R95, we describe a new Global Average Ionosphere/Thermosphere (GAIT) model that represents the average state of the atmosphere, from the mesopause to upper thermospheric heights. In addition to the three major neutral species, N_2, O_2, and O, the model also solves for the concentrations of various minor neutral constituents; these include, He, $N(^4S)$, NO, and CO_2, which are subject to transport, and O_3, $O(^1D)$, $O_2(^1\Delta g)$, $O_2(^1\Sigma_g)$, and $N(^2D)$, all of which are assumed to be in photochemical equilibrium. In the ionosphere, the model includes five different ion species and two excited states of O^+; $O^+(^4S)$ and N^+ are subject to transport, while the remaining ions, O_2^+, NO^+, N_2^+, $O^+(^2D)$, and $O^+(^2P)$, are assumed to be in photochemical equilibrium.

[6] Given our eventual goal of exploring the upper atmosphere's response to irradiance inputs outside of the normal solar cycle, the GAIT model is built to be largely independent of a specific solar irradiance representation. For example, rather than using volume heating rates parameterized by the 10.7 cm radio flux (F10.7), we directly account for the photon flux between 3 and 360 nm. The

[1]Now at Air Force Institute of Technology, Wright-Patterson Air Force Base, Ohio, USA.

0148-0227/05/2004JA010781$09.00

GAIT model also includes an approximate treatment of photoelectrons, rather than relying on simple scale factors of secondary ionization or parameterizations of the thermal electron volume heating rate.

[7] In this paper we describe the GAIT model in detail and then validate our results against the earlier *Roble et al.* [1987] model, as well as the Mass Spectrometer Incoherent Scatter (MSIS-90) empirical model [*Hedin*, 1991]. We next examine the model's sensitivity to uncertainties in key reaction rates and inputs affecting the global energy budget. Leveraging the GAIT model's sensitivity to the input solar spectrum, we explore its response to four different extreme ultraviolet (EUV) irradiance models. We find that one of the irradiance models does not have sufficient dynamic range to reproduce the expected variation in the neutral gas temperature. We conclude with a discussion of the wavelength sensitivity of model results.

[8] A companion paper uses the GAIT model to examine the response of the coupled thermosphere and ionosphere to irradiance input outside of the normal solar cycle range. In one extreme, we reduce the input solar irradiance toward levels believed representative of the Maunder Minimum epoch (1640–1710 A.D.), and in the other we extrapolate to extremely high levels; the solar irradiance is increased by an amount equal to three times the normal cycle variation.

2. GAIT Model Description

[9] The GAIT model self-consistently solves the one-dimensional neutral, ion, and electron energy equations, as well as the continuity and momentum equations for both neutral and ion species. The lower boundary is set to an altitude of 95 km, while the upper boundary is varied to capture the topside *F* region ionosphere, typically between 500 and 700 km. Beginning with arbitrary initial conditions, the coupled equations are integrated forward in time until the system reaches a steady state, in approximately 20 days of integration time.

[10] The model description given in this section focuses primarily on processes that have been updated or otherwise differ from the earlier models in R87 and R95. The first and most obvious distinction being the GAIT model is solved in Cartesian altitude coordinates, while the earlier models were solved in pressure coordinates. Transforming from altitude to pressure is simple, and we will, in fact, present most of the output in pressure coordinates in order to facilitate comparison with the earlier results.

2.1. Neutral Gas Energy Equation

[11] The familiar heat conduction equation is modified to approximate the effects of turbulent mixing [*Johnson and Gottlieb*, 1970; *Gordiets et al.*, 1982],

$$C_p n \frac{\partial T}{\partial t} - \frac{\partial}{\partial z}\left(C_p n K_{eddy}\left(\frac{\partial T}{\partial z} + \Gamma\right) + \lambda \frac{\partial T}{\partial z}\right) = Q - L \qquad (1)$$

where T and n identify the neutral gas temperature and density, Γ the adiabatic lapse rate ($\sim$10 K/km), K_{eddy} the eddy diffusion coefficient, and z the altitude. C_p and λ (refer to the specific heat and thermal conductivity [*Schunk and Nagy*, 2000], averaged for a multispecies gas. Q and L are the heating and cooling terms described further in sections 2.5 and 2.6.

[12] The temperature at the model's lower boundary is fixed at 177 K, on the basis of a global average obtained from the empirical MSIS-90 model. The model's lower boundary height was deliberately chosen to coincide with the global average mesopause height, since the MSIS-90 global average temperature changes less 1% over the course of the solar cycle at this altitude. At the upper boundary we assume $\frac{\partial T_n}{\partial z} = 0$.

[13] No standard formulation for the shape or magnitude of the eddy diffusion coefficient exists; it remains essentially a free parameter used to match model with observations in the mesosphere and lower thermosphere. We followed the parameterization of R87,

$$K_{eddy}(Z) = K^{\max} \mathrm{Exp}[-7 - Z] \qquad (2)$$

A maximum value of $K^{\max} = 100\ \mathrm{m^2\ s^{-1}}$ was selected in order to best match MSIS-90 global averages. The independent variable Z is a pressure coordinate defined in R87 as

$$Z = \mathrm{Log_e}[P_o/P] \qquad (3)$$

where P is the pressure, and the reference pressure P_o is 50 μPa.

2.2. Ion and Electron Energy Equations

[14] For the parallel ion and electron temperatures an equation similar to (1) applies, but because T_i and T_e are locked to T_n at low altitudes, we can neglect the eddy diffusion term [*Schunk and Nagy*, 2000]. Calculation of the thermal conductivities for both the ion and electron equations are described in *Rees and Roble* [1975] and *Schunk and Nagy* [2000]. Thermal electrons are heated by collisions with photoelectrons, described further in section 2.8. Collisional heating and cooling rates for the ion and electron gases are given by *Schunk* [1988], *Schunk and Nagy* [2000], and *Rees and Roble* [1975].

[15] At the lower boundary, both the electron and ion temperatures are set equal to the neutral temperature. A downward heat flux from field lines connecting to the plasmasphere and magnetosphere is required to obtain a reasonable electron temperature profile; R87 and R95 adopt a fixed heat flux boundary condition of 3×10^9 eV cm^{-2} s^{-1} for the electron gas. To better approximate variation during the solar cycle we have used the *Titheridge* [1998] empirical model to create global average electron temperature profiles, and from these profiles generated a simple linear relationship for the heat flux as a function of solar cycle. This parameterization results in a heat flux of 4.4 and 7.2×10^9 eV cm^{-2} s^{-1} at solar minimum and maximum respectively. For the ions we use a free upper boundary condition, $\frac{\partial^2 T_i}{\partial z^2} = 0$.

2.3. Momentum and Continuity Equations

[16] The momentum equation for the neutral constituents follows from the development of *Chapman and Cowling* [1952]; *Colegrove et al.* [1966] later included a term to approximate the effects of eddy diffusion. The resulting

Table 1. Updated Neutral-Neutral Chemistry

Reaction	Reaction Rate
$O(^1D) + O_2 \xrightarrow{k1} O + O_2(^1\Sigma_g) + 0.34$ eV	$k_1 = 2.46 \times 10^{-11}$ Exp[70/T] [a,b]
$O(^1D) + O_2 \xrightarrow{k2} O + O_2 + 1.97$ eV	$k_2 = 7.35 \times 10^{-12}$ Exp [70/T] [a,b]
$O_2(^1\Delta_g) + O_2 \xrightarrow{k3} O_2 + O_2 + 0.98$ eV	$k_3 = 3.6 \times 10^{-18}$ Exp[−220/T] [a]
$O(^1D) \xrightarrow{A4} O + h\nu$	$A_4 = 8.33 \times 10^{-3}$ s^{-1} [c]
$NO + N(^4S) \xrightarrow{k5} N_2 + O + 2.68$ eV	$k_5 = 2.1 \times 10^{-11}$ Exp[100/T] [a]
$N(^2D) + O \xrightarrow{k6} N(^4S) + O + 2.38$ eV	$k_6 = 6.9 \times 10^{-13}$ [d]

[a] *JPL* [2003].
[b] *Mlynczak and Solomon* [1993].
[c] *Nee and Lee* [1997].
[d] *Fell et al.* [1990].

one-dimensional equation for component i of a multispecies gas, neglecting bulk motion, can be written as,

$$\varphi_i = -D_i\left(\frac{\partial n_i}{\partial z} + \frac{n_i}{H_i} + (1+\alpha_i)\frac{n_i}{T}\frac{\partial T}{\partial z} - n_i\sum_{j\neq i}\frac{\varphi_j}{ND_{ij}}\right) - K_{eddy}\left(\frac{\partial n_i}{\partial z} + \frac{n_i}{H_{mix}} + \frac{n_i}{T}\frac{\partial T}{\partial z}\right) \quad (4)$$

where n_i, φ_i, and α_i identify the concentration, flux, and thermal diffusion factor of species i respectively. The thermal diffusion factor is assumed to be zero for all species except helium, for which it is set to −0.4 [*Colegrove et al.*, 1966]. H_i is the scale height of species i, while H_{mix} is the scale height of the mixture. The diffusion coefficient D_i is given by

$$D_i \equiv \left(\sum_{j\neq i}\frac{n_j}{ND_{ij}}\right)^{-1} \quad (5)$$

The mutual diffusion coefficient D_{ij} is a function of temperature. When available, experimental results are used [*Colegrove et al.*, 1966]; otherwise we rely on the hard sphere approximation and estimates of the collision diameter given by *Lettau* [1951]. When applying (4) and (5) to minor neutral species, the sum j is over just the three major constituents.

[17] The flux, φ_i, specified by the momentum equation above is substituted into the continuity equation,

$$\frac{\partial n_i}{\partial t} = P_i - L_i n_i - \frac{\partial \varphi_i}{\partial z} \quad (6)$$

P_i and L_i are the constituent dependent production and loss terms, which include photodissociation, photoionization, and the applicable chemical reactions. The model's chemical scheme is primarily a subset of the one given in R95, where we have used only those reactions relevant to the constituents included in the GAIT model. A few additional reactions have also been included, primarily on the basis of the ionospheric scheme of *Schunk* [1988]; updates have also been made to reaction rates when available. Tables 1 and 2 list those reactions and reaction rates that differ from the chemistry of R95.

Table 2. Updated Ion-Neutral Chemistry

Reaction	Reaction Rate
$O^+ + NO \xrightarrow{\gamma 1} NO^+ + O + 4.36$ eV	$\gamma_1 =$ (i) [a,b]
$O_2^+ + N(^4S) \xrightarrow{\gamma 2} NO^+ + O + 4.21$ eV	$\gamma_2 = 1.5 \times 10^{-10}$ [c]
$O_2^+ + N_2 \xrightarrow{\gamma 3} NO^+ + NO + 0.93$ eV	$\gamma_3 = 5. \times 10^{-16}$ [b]
$N_2^+ + O_2 \xrightarrow{\gamma 4} O_2^+ + N_2 + 3.53$ eV	$\gamma_4 = 5 \times 10^{-11}\,(300/T_i)$ [b]
$N_2^+ + O \xrightarrow{\gamma 5} O^+ + N_2 + 1.96$ eV	$\gamma_5 = \begin{cases} 1 \times 10^{-11}(300/T_i)^{0.23}; & T_i \le 1500 \\ 3.62 \times 10^{-12}(T_i/300)^{0.41}; & T_i > 1500 \end{cases}$ [c]
$N^+ + O_2 \xrightarrow{\gamma 6} O_2^+ + N(^2D) + 0.1$ eV $\rightarrow O_2^+ + N(^4S) + 2.49$ eV	$\gamma_6 = 3.07 \times 10^{-10}$; Yield (0.66/0.33) [d]
$N^+ + O_2 \xrightarrow{\gamma 7} NO^+ + O + 6.67$ eV	$\gamma_7 = 2.32 \times 10^{-10}$ [c]
$O_2^+ + e^- \xrightarrow{\gamma 8} O(^3P) + O(^3P) + 6.99$ eV $\rightarrow O(^3P) + O(^1D) + 5.02$ eV $\rightarrow O(^1D) + O(^1D) + 3.06$ eV	$\gamma_8 = \begin{cases} 1.95 \times 10^{-7}(300/T_e)^{0.7}; & T_e \le 1200 \\ 7.38 \times 10^{-8}(1200/T_e)^{0.56}; & T_e > 1200. \end{cases}$ Yield (0.22, 0.42, 0.36) [c]
$N_2^+ + e^- \xrightarrow{\gamma 9} N(^4S) + N(^2D) + 3.44$ eV $\rightarrow N(^4S) + N(^4S) + 5.82$ eV	$\gamma_9 = 2.2 \times 10^{-7}\,(300/T_e)^{0.39}$ Yield(0.9/0.1) [c]

[a] (i) $= \begin{cases} 8.36 \times 10^{-13} - 2.02 \times 10^{-13}T_x + 6.95 \times 10^{-14}T_x^2 & 320 \le T_i \le 1500 \\ 5.33 \times 10^{-13} - 1.64 \times 10^{-14}T_x + 4.72 \times 10^{-14}T_x^2 - 7.05 \times 10^{-15}T_x^3 & 1700 > T_i > 6000 \end{cases}$
Where $T_x = T_i/300$
[b] *Schunk* [1988, and references therein].
[c] *Schunk and Nagy* [2000].
[d] *Rees* [1989].

[18] When solving the coupled continuity and momentum equations, diffusive equilibrium is imposed at the upper boundary. The lower boundary condition depends on the species. N_2 and O_2 concentrations are fixed at 2.28×10^{13} cm^{-3} and 5.72×10^{12} cm^{-3} on the basis of globally averaged MSIS-90 results. As noted previously, these boundary conditions vary on the order of 1% over the course of the solar cycle, reflecting stability of the lower atmosphere. The globally averaged atomic oxygen profile calculated by MSIS-90 peaks in the vicinity 95 km, and we therefore assume a lower boundary condition of $\partial[O]/\partial z = 0$ for atomic oxygen.

[19] Of the ions, $O^+(^4S)$ and N^+ are subject to transport, the rest are assumed to be in photochemical equilibrium. The ion momentum equation is similar to (4), with the diffusion coefficient, scale height, and neutral temperature replaced by equivalent plasma parameters [*Schunk*, 1988; *Schunk and Nagy* 2000]. Photochemical equilibrium is assumed as a lower boundary condition for all species. NO^+, O_2^+, and N_2^+ are coupled nonlinearly through dissociative recombination reactions with electrons; to facilitate a stable solution, the corresponding continuity equations are expanded in a Taylor's series using the method described by *Schunk* [1988].

2.4. Solar Irradiance

[20] R87 relied on measurements from the Atmospheric Explorer (AE) satellites made during solar minimum and maximum to specify the solar irradiance [*Torr and Torr*, 1980, 1985; *Hinteregger et al.*, 1981]. Since that time, additional measurements and improved instrument calibration have resulted in new empirical solar irradiance models. R95 accounted for these updates by including an unpublished irradiance model developed by S. C. Solomon. The standard irradiance input for the GAIT model is based on the vacuum ultraviolet (VUV) model [*Woods and Rottman*, 2002], and is described further in section 5. For convenience, we will refer to the ionizing wavelengths, 3–105 nm, as the EUV, and everything longward of 105 nm as UV.

2.5. Neutral Gas Heating

[21] The global average heating rate, Q in equation (1), consists of a number of different processes: (1) excess energy available after photon dissociation, (2) heating from exothermic neutral-neutral chemical reactions, including recombination of atomic oxygen and quenching of excited species, (3) heating from exothermic ion-neutral chemical reactions, (4) collisions between thermal electrons, ions, and neutrals, and (5) Joule heating. All but one of these processes (Joule heating) begins with the absorption of solar photons.

[22] In the global average, the effective photoabsorption rate at altitude z, by species i, is given by the expression,

$$\bar{J}_i(z) = \frac{1}{2}\int_{-1}^{1} d\mu n_i(z) \int_{\lambda} d\lambda I_\infty(\lambda)\sigma_i(\lambda)\mathrm{Exp}[-\tau(\lambda,\mu,z)] \quad (7)$$

Here n_i is the concentration and σ_i the absorption cross section of species i; I_∞ identifies the solar flux at the top of the atmosphere and τ the optical depth, which is calculated using the method of *Smith and Smith* [1972]. In the above expression, the outer integration is over the cosine of the solar zenith angle μ, and the inner integration is over λ, the incident wavelength. Equation (7) differs from the one used in R87 and R95. That earlier work assumed a "plane atmosphere" to simplify the expression; however, this assumption breaks down for latitudes higher than ~70 degrees resulting in lower photoabsorption rates than those calculated with (7).

[23] *Torr et al.* [1979] parameterized the EUV wavelengths, from 5 to 105 nm, into 37 wavelength bins and provided effective absorption and ionization cross sections; these flux averaged cross sections were updated by *Richards et al.* [1994] to include the more recent measurements compiled by *Fennelly and Torr* [1992]. The GAIT model extends the coverage down to 3 nm using the Fennelly and Torr data.

[24] The model includes the effects of the strong H Lyman-alpha line (121.6 nm) using the cross sections parameterized by *Nicolet* [1985]. In the Schumann-Runge continuum (125–175 nm), the photons are absorbed primarily by O_2, resulting in dissociation into $O(^3P)$ and $O(^1D)$. Absorption cross sections in this wavelength region are from *Strobel* [1978] and the quantum yield for production of $O(^1D)$ comes from *Nee and Lee* [1997] and *Lee and Nee* [2000].

[25] Calculation of the O_2 photodissociation rate in the Schumann-Runge bands (175–195 nm) is complicated by a highly variable O_2 absorption cross section. Under these circumstances, averages made over the 1–5 nm wide bins we typically use are no longer physically representative of the actual cross section, and the problem seemingly requires high-resolution integration over wavelength. A computationally efficient alternative is to transform the highly variable integrand into a smooth one using a cumulative distribution function, as described by *Minschwaner et al.* [1993]. At these longer wavelengths the products of O_2 dissociation are all assumed to be in the ground state, $O(^3P)$.

[26] Longward of 195 nm, absorption by O_2 is negligible in the thermosphere, but photolysis of ozone in the Hartley (200–300 nm) and Huggins (300–350 nm) bands contributes a small amount to the total neutral gas heating rate. Ozone photoabsorption cross sections and the quantum yield for excited state dissociation products are taken from *Jet Propulsion Laboratory* (*JPL*) [2003].

[27] *Roble and Emery* [1983] found that the global average exosphere temperature they calculated was too small without the addition of a high-latitude heat source, to account for Joule heating and auroral particle input. On the basis of the results of R87 we represent quiet geomagnetic conditions using a fixed global Joule heating rate of 70 GW, and disregard the negligible direct particle heating. The heating rate is calculated using the following expression,

$$Q_{Joule} = \sigma_p E^2 \quad (8)$$

where σ_p is the Pedersen conductivity and E an imposed electric field that is assumed constant in height. To account for changes in σ_p, the applied electric field is updated at each integration step ensuring the integrated Joule heating rate remains constant.

2.6. Neutral Gas Cooling

[28] The loss term, L, in equation (1) is composed of three infrared radiative cooling mechanisms: (1) 63 μm cooling

due to the fine structure of atomic oxygen, (2) 5.3 μm cooling from the fundamental band of nitric oxide, and (3) cooling due to the 15 μm band of carbon dioxide.

[29] *Bates* [1951] was the first to demonstrate the importance of infrared cooling at 63 μm, using a local thermodynamic equilibrium (LTE) expression and assuming an optically thin atmosphere. At low altitudes, however, the thermosphere is optically thick to 63 μm. A parameterization by *Glenar et al.* [1978] is used to approximate the necessary correction, giving nearly the same results as full radiative transfer calculations based on the algorithms of *Craig and Gille* [1969] and *Kockarts and Peetermans* [1970].

[30] In R87, Roble et al. arbitrarily reduced the 63 μm cooling rate by a factor of 2 in order to approximate non-LTE effects suggested by the results of *Grossmann and Offermann* [1978] and *Durrance and Thomas* [1979]. However, more recent measurements by *Grossmann and Vollmann* [1997] and modeling work by *Sharma et al.* [1994] provided evidence for an LTE distribution through most of the thermosphere; therefore the GAIT model uses the LTE assumption. If we instead adopt the approach of R87, and divide the 63 μm cooling rate by a factor of 2, the resulting exospheric temperatures are 4% higher at solar minimum and 2% higher at maximum.

[31] *Kockarts* [1980] showed that the fundamental 5.3 μm NO emission is not in local thermodynamic equilibrium, and used detailed balance to derive an expression for the population of NO in the $\nu = 1$ vibrational level. Collisions between NO and O are the most important in exciting this state, and we adopt a value of 2.8×10^{-11} cm^3 s^{-1} [*Duff and Sharma*, 1997] for this rate coefficient.

[32] Cooling by CO_2 at 15 μm requires both a consideration of non-LTE effects as well as radiative transfer; in addition, closely spaced energy levels and differences between CO_2 isotopes makes it the most difficult of the three radiative processes to model. The parameterization of *Fomichev et al.* [1998], which is used in the GAIT model, takes into account these processes. As was the case with NO, collisions involving O are the most important means of exciting this CO_2 vibrational state. There is significant uncertainty in the rate coefficient for these collisions; we use the rate suggested by *Sharma and Wintersteiner* [1990] and discuss the model's sensitivity to this rate further in section 4.1.

2.7. Minor Neutral Constituents

[33] The metastable states of atomic and molecular oxygen, $O(^1D)$, $O_2(^1\Delta_g)$, and $O_2(^1\Sigma_g)$, are assumed to be in photochemical equilibrium. These excited state species are produced primarily during the dissociation of O_2 and O_3 by ultraviolet radiation, and are included in order to obtain the correct heating efficiency [*Mlynczak and Solomon*, 1993].

[34] Ozone is included in the model for its minor role in neutral gas heating. On the basis of the results of *Allen et al.* [1984], we assume O_3 is in photochemical equilibrium. Photolysis cross sections and quantum yields for excited state products are taken from *JPL* [2003].

[35] The carbon dioxide concentration is of great importance given its role in cooling the neutral gas. On the basis of the work of *Trinks and Fricke* [1978], carbon dioxide is subject to vertical transport. CO_2 photoabsorption cross sections used in the GAIT model are taken from *Yoshino et al.* [1996], *Shemansky* [1972], and *Nicolet* [1985]. Because global empirical models for the CO_2 concentration do not exist, the lower boundary condition is specified using a fit to experimental data provided by *Fomichev et al.* [1998], which corresponds to a mixing ratio of 360 ppm in the homosphere. For comparison, R95 specified 350 ppm as a global average boundary condition at 30 km. Although there is some uncertainty in the proper mixing ratio, the model results are relatively insensitive to it. Varying the homosphere mixing ratio from 300 to 400 ppm, results in a 3.5% change to the neutral exospheric temperature at solar minimum, and only 1% at solar maximum when cooling by NO compensates.

[36] In order to calculate the nitric oxide concentration, an important contributor to radiative cooling, we must also account for both ground state and metastable atomic nitrogen, $N(^4S)$ and $N(^2D)$. The concentrations of NO and $N(^4S)$ are modeled as minor species subject to transport, whereas photochemical equilibrium is assumed for $N(^2D)$. Photolysis of NO in the Schumann-Runge bands is included using the method of *Minschwaner and Siskind* [1993]. At the lower boundary we use the approach of R87; $N(^4S)$ is assumed to be in photochemical equilibrium, while for NO we allow a small downward flux. Other than to generate a physically satisfying low altitude profile for NO, the choice of downward flux is irrelevant; cooling by CO_2 dominates at the model's lower boundary, and the choice of flux does not affect higher altitudes where cooling by NO is important.

[37] Helium is included in the model as a passive tracer. Its vertical distribution is governed solely by diffusive transport, both eddy and molecular. The vertical profile is used to help tune the eddy diffusion coefficient through comparison with the MSIS-90 model. At high altitudes, He also contributes to the diffusion coefficient and thermal conductivity.

2.8. Photoelectrons

[38] Photoelectrons provide the primary heat source for thermal electrons, as well as an important source of secondary ionization to the neutrals. R87 and R95 relied on a parameterization by *Swartz and Nisbet* [1972] to specify the thermal electron heating rate as a function of the total photoionization rate, and assumed secondary ionization to be 30% of the primary EUV ionization rate. While reasonably accurate under normal solar conditions, both of these parameterizations are based on an assumed solar spectrum and therefore cannot reflect gross changes for extreme solar input or variability in the spectral weighting between various spectra.

[39] Rather than rely on parameterizations to account for photoelectrons, the GAIT model includes an approximate solution for the photoelectron flux based on the model of *Richards and Torr* [1983]. Their approach uses a local equilibrium approximation to calculate the photoelectron flux at each altitude. The treatment of cascading electrons is simplified by assuming only a limited set of energy losses available to each electron based on the average losses for that particular energy. Excitation and ionization cross sections are derived from the early parameterizations of *Green and Stolarski* [1972] and *Jackman et al.* [1977]; *Solomon et*

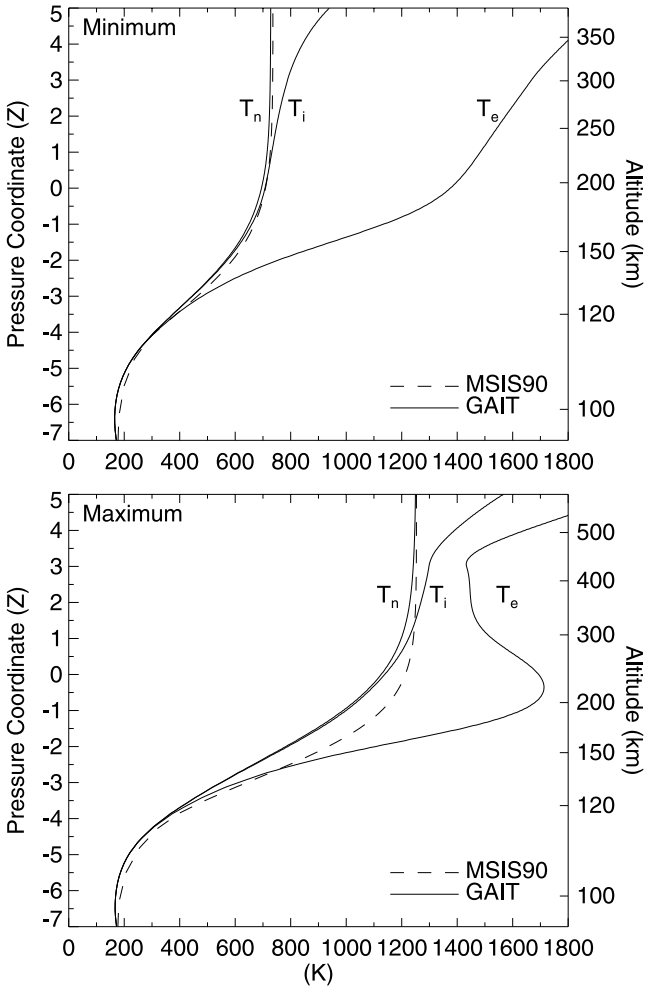

Figure 1. Global mean temperature profiles calculated using the GAIT model (solid lines) and MSIS-90 empirical model (dashed line). The three profiles correspond to neutral (T_n), ion (T_i), and electron (T_e) gases. (top) Solar minimum and (bottom) solar maximum assuming quiet geomagnetic conditions (Ap = 4).

al. [1988] updated the coefficients to include more recent measurements.

[40] Using their local equilibrium approximation, *Richards and Torr* [1983] were able to show excellent agreement with a full transport model across all energies for altitudes below 250 km, and reasonable agreement with observations from the AE-E satellite. Above 300 km, transport effects become increasingly important and the approximation overestimates the photoelectron flux, especially at energies below 20 eV. For this reason, the GAIT model does not include photoelectron effects above a pressure coordinate of Z = 3 (300–400 km). This approach causes a small discontinuity in some of the minor neutral and ion constituents and an inflection in the electron temperature profile, but neither significantly affects the overall solution.

[41] *Richards and Torr* [1983] cautioned that the photoelectron flux below 2 eV, which is responsible for most of thermal electron heating, may be too high at all altitudes because of transport effects. In fact, the electron heating rate calculated in the GAIT model is 40% higher than the *Swartz and Nisbet* [1972] parameterization at the peak heating altitude, although some of this difference could be attributed to updated cross sections. On the other hand, the ratios of photoelectron to primary ionization rates calculated by the GAIT model are remarkably similar to those given by *Richards and Torr* [1988] based on a full transport solution.

3. Model Validation

[42] The GAIT model was run using the inputs described previously for both solar minimum and maximum, assuming quiet geomagnetic conditions (Ap = 4). Per the arguments of R87, the applied electric field associated with Joule heating was set such that it resulted in 70 GW of global heat input. Other than changing the input solar irradiance, specified by the VUV model, all other input conditions remained fixed between the two runs. All of the profiles shown here (Figures 1–4) are plotted using the pressure coordinate Z as the vertical axis in order to facilitate comparisons with R87 and R95.

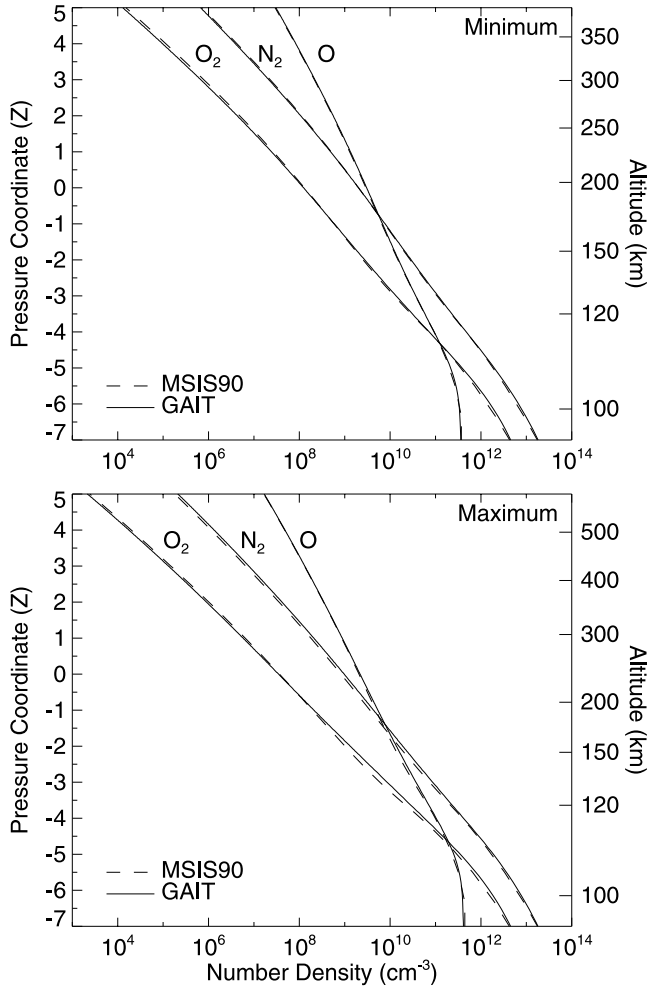

Figure 2. Global mean number density profiles for the three major neutral species (N_2, O_2, and O) calculated using the GAIT model (solid lines) and MSIS-90 empirical model (dashed lines). (top) Solar minimum, and (bottom) solar maximum assuming quiet geomagnetic conditions (Ap = 4).

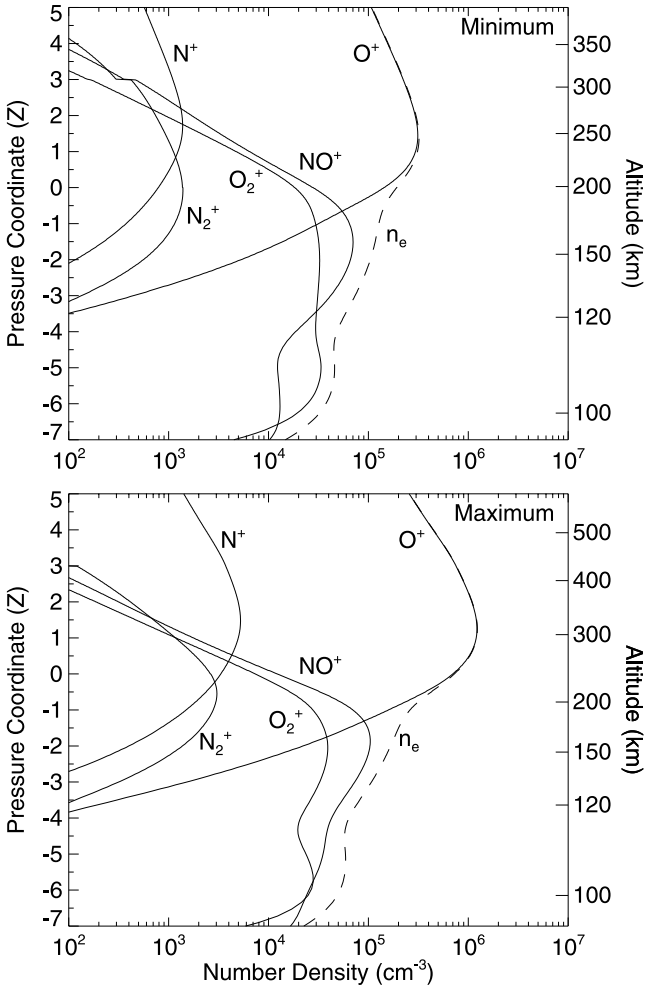

Figure 3. Global mean number density profiles for five ion species (O^+, NO^+, O_2^+, N^+, and N_2^+) and the total electron density (n_e) calculated using the GAIT model. (top) Solar minimum and (bottom) solar maximum assuming quiet geomagnetic conditions (Ap = 4). The discontinuity observed in the NO^+ and N_2^+ profiles at Z = 3 corresponds to where the photoelectron calculation stops.

[43] Given the long time constants of the thermosphere, the GAIT modeled temperature and neutral gas concentrations are reasonably representative of the average conditions, since these parameters undergo relatively little diurnal variation. On the other hand, time constants in the ionosphere are shorter, and there is typically a strong diurnal variation in the electron density and plasma temperature. The concept of a globally averaged ionosphere is therefore not as intuitive. Because the solar input is ever-present, yet reduced by averaging, it is more appropriate to think of the ionosphere calculated by the GAIT model as representing midlatitude daytime conditions, subject to the underlying modeled thermosphere. Indeed, ion concentrations calculated by the GAIT model are very similar to midlatitude daytime results from other 3-D physical models, such as the Time-Dependent Ionosphere Model [*Schunk*, 1988].

3.1. Neutral, Ion, and Electron Gas Temperatures

[44] Figure 1 shows the calculated neutral, ion, and electron gas temperature profiles for both solar minimum (Figure 1, top) and maximum (Figure 1, bottom). Also shown are the globally averaged neutral temperature profiles from the empirical MSIS-90 model.

[45] At solar minimum the GAIT model calculated an exospheric temperature of 728 K compared to an MSIS-90 value of 736 K. As Figure 1 demonstrates, the two solar minimum temperatures correlate extremely well over the entire profile. The solar minimum ion and electron temperature profiles are also very similar in both shape and magnitude to those of R87. At Z = 5 (∼400 km) the electron temperature calculated by the GAIT model is 1920 K compared to approximately 1775 K calculated in R87, but this is to be expected given the differences in the electron heat flux boundary condition.

[46] The GAIT model calculated a solar maximum exospheric temperature of 1250 K versus an MSIS-90 value of 1253 K; however, as Figure 1 (bottom) shows, the two temperature profiles do not track as closely as in the solar minimum case. At a pressure of Z = −1.5 (∼175 km) the MSIS-90 temperature is nearly 17% greater than the GAIT

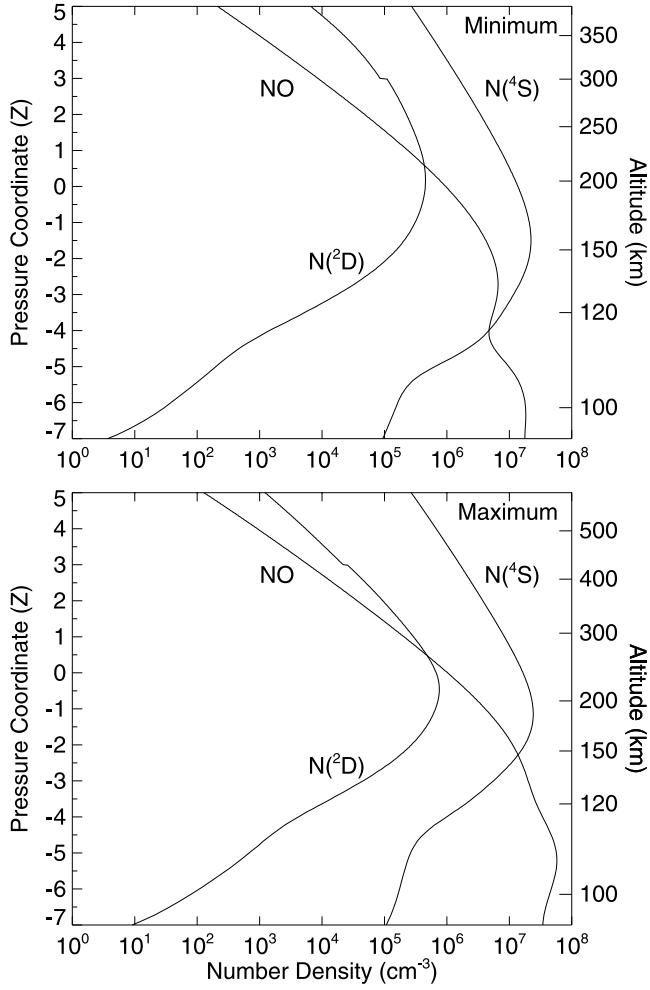

Figure 4. Global mean number density profiles for the odd nitrogen species ($N(^4S)$, $N(^2D)$, and NO) calculated using the GAIT model. (top) Solar minimum and (bottom) solar maximum assuming quiet geomagnetic conditions (Ap = 4). The discontinuity observed in the NO profile at Z = 3 corresponds to where the photoelectron calculation stops.

result. As we describe later, significant uncertainty remains in some of the important reaction rates, as well as the choice of EUV representation, all of which could contribute to this discrepancy.

[47] The calculated ion and electron temperature profiles at solar maximum are again similar to those of R87. A peak in the electron temperature at approximately 200 km corresponds to a maximum in photoelectron heating. The electron temperature at this local maximum is about 15% larger than the Roble et al. value, reflecting the fact that the photoelectron heating rate calculated internally by the GAIT model is about 40% higher than the one used in R87. Above this peak, the electron temperature decreases to come within roughly 200 K of the neutral temperature. This reflects increased collisional coupling between electrons, ions, and neutrals at these altitudes, which is greater at solar maximum than minimum because of the increased electron density. As was the case for solar minimum, the GAIT electron temperature is much higher than R87, 2024 K versus ~1700 K, again because of the difference in the electron heat flux boundary condition. The solar maximum electron temperature profile shows a small inflection at Z = 3 coinciding with where the photoelectron calculation stops, while in the solar minimum case, the downward heat flux dominates, resulting in a smooth profile.

3.2. Major Neutral Constituents

[48] Global mean number densities for the three major neutral species are shown in Figure 2, along with similar global means from the MSIS-90 model. Viewed on a log scale, the two models appear to agree remarkably well over the entire altitude range and at both solar minimum and maximum. At solar minimum the largest difference between the GAIT and MSIS-90 results are in O_2, which differ by 16% at Z = 3.5. The maximum difference in the N_2 and O profiles at solar minimum are 9% and 5%. The close agreement between the atomic oxygen profiles is especially good considering that it uses a Neumann lower boundary condition rather than one specified by MSIS-90. The agreement between the GAIT and MSIS-90 models is not quite as good at solar maximum, which should be expected given the differences that exist in the neutral temperature profile (Figure 1). The largest variation between the two models is again found in the O_2 profile, which shows a 44% difference at Z = −3. The maximum differences in the N_2 and O profiles are 21% and 16% respectively, at roughly the same pressure.

3.3. Ionospheric Constituents

[49] Figure 3 shows the calculated global mean electron and ion density profiles for both solar minimum and maximum. It is important to reiterate that the timescales in the ionosphere are too short to justify the concept of a "global mean," as opposed to the thermosphere where this makes physical sense. Instead, given the commensurate reduction of photon flux, the ion and electron density profiles computed by GAIT should be taken to represent daytime midlatitude conditions, subject to the underlying global average thermosphere.

[50] In Figure 3, a discontinuity in the NO^+ and N_2^+ concentrations at Z = 3 corresponds to where the photoelectron calculation stops, which reduces the effective ionization rate. A discontinuity also exists in the O_2^+ profile, but it is too small to be visible. Transport smoothes out any discontinuities in the $O^+(^4S)$ and N^+ profiles. Fixed scale factors could be used to approximate secondary ionization above Z = 3, but the discontinuities are retained to both remind us of where the photoelectron calculation stops, as well as to indicate the magnitude of the effect they have on the total concentration. At solar minimum, eliminating the secondary ionization source decreases the N_2^+ and NO^+ densities by 27% and 21% respectively, while O_2^+ only decreases by 6%. The discontinuities at solar maximum are not visible in Figure 3, however, the N_2^+, NO^+, and O_2^+ concentrations decrease by 21%, 5%, and 6% respectively.

[51] The results shown in Figure 3 are consistent with the previous global average results of R87 and R95. Some differences exist, particularly in the *E* region concentrations of NO^+ and O_2^+ during solar maximum, where variability in solar soft X-rays and the impact of photoelectrons are important.

3.4. Minor Neutral Constituents

[52] Figure 4 shows the calculated global mean densities for the odd nitrogen family, $N(^4S)$, $N(^2D)$, and NO, at both solar minimum and maximum. Once again, at Z = 3 the concentration of $N(^2D)$, which depends strongly on ion chemistry, shows a discontinuity where secondary ionization by photoelectrons artificially stops. The primary sources of NO are the reaction of $N(^2D)$ with O_2 at low altitudes and $N(^4S)$ with O_2 at higher altitudes. The second of these reactions is highly dependent on temperature; as a result, the shape of the NO profile shows distinct differences between solar minimum and maximum at roughly Z = −4 (115 km). These changes relate directly to the neutral temperature; even a small increase in the temperature at these altitudes, e.g., an additional 25 K caused by increasing the Joule heating rate to 100 GW, removes the dip at Z = −4.

4. Model Sensitivities

[53] We next examine the GAIT model's sensitivity to key heating and cooling processes by considering uncertainties in the reaction rates and inputs. The neutral gas exospheric temperature and total electron content (TEC) are chosen as scalar variables representative of the thermosphere and ionosphere respectively. The total electron content is approximated by integrating the electron density over the model's altitude range and then adding a topside contribution by assuming the electron density extends to infinity at the O^+ scale height. Table 3 lists the percentage change that occurs in both. The reference values, using the standard inputs described previously, are listed as case a.

4.1. CO_2 Cooling

[54] Radiative cooling at 15 μm by CO_2 constitutes roughly 60% of the total heat loss in the thermosphere, therefore changes to this process can have a dramatic effect on the global average solution. The bending vibration responsible for the 15 μm emission is excited primarily by collisions between CO_2 and O, but the reaction rate for this collision has a large uncertainty. The only experimental results suggest a value of roughly 1×10^{-12} cm^3 s^{-1} [*Shved et al.*, 1991; *Pollock et al.*, 1993], while *Sharma and*

Table 3. Sensitivity of the Modeled Thermospheric Temperature and Total Electron Content to Key Reaction Rates and Inputs

		% Difference From Reference			
		Exospheric Temperature, K		Total Electron Content, 10^{16} m^{-2}	
Case	Description	Solar Minimum	Solar Maximum	Solar Minimum	Solar Maximum
a	reference values	728	1250	6.8	37.5
b	reaction rate for CO_2-O excitation of bending vibration: $5.77 \times 10^{-14} \sqrt{T_n}$ cm^3 s^{-1}	+11.9	+4.2	+22.6	+10.0
c	reaction rate for N(^{4}S) + NO: $k_{14} = 3.4 \times 10^{-11}$ cm^3 s^{-1}	+1.0	+3.4	+1.5	+3.3
d	reaction rate for N(^{4}S) + NO: $k_{14} = 1.6 \times 10^{-10}$ Exp[$-460/T_n$] cm^3 s^{-1}	+2.9	+12.7	+4.2	+10.3
e	40 GW of global Joule heating	−4.8	−3.3	−6.9	−4.7
f	100 GW of global Joule heating	+4.7	+3.1	+5.5	+2.6
g	electron gas heat flux boundary condition: 3×10^9 eV cm^{-2} s^{-1}	−0.5	−1.8	−2.5	−0.1
h	secondary ionization scale factor	−1.4	−2.9	−2.9	−8.3
i	parameterized electron gas volume heating	−1.3	−6.2	−3.1	−7.1

Wintersteiner [1990] estimated a room temperature value of 6×10^{-12} cm^3 s^{-1} based on model fits to satellite measurements; the standard GAIT model uses the *Sharma and Wintersteiner* [1990] coefficient. Case b in Table 3 shows the change that occurs if we adopt the lower experimental value. At solar minimum the exospheric temperature increases by almost 12%; at solar maximum the percentage increase is less because cooling by NO is more effective.

4.2. NO Cooling

[55] Emission at 5.3 μm by NO is an important thermospheric cooling mechanism, especially for high solar activity. The principal loss for NO is the reaction NO + N(^{4}S) → N_2 + O; however, the temperature dependence of this reaction rate differs significantly in the literature [*Wennberg et al.*, 1994]. The GAIT model uses the value recommended by *JPL* [2003], 2.11×10^{-11} Exp[100/T_n] cm^3 s^{-1}, while R87 used a constant value of 3.4×10^{-11} cm^3 s^{-1} and R95 used a value of 1.6×10^{-10} Exp[−460/T_n] cm^3 s^{-1}, which has a completely different temperature dependence than the JPL coefficient. Cases c and d in Table 3 examine the sensitivity of the GAIT model to these different reaction rates. In both examples, the changes lead to increased exospheric temperatures and TEC.

4.3. Joule Heating

[56] In R87, Roble et al. suggested that a global Joule heat input of 70 GW was consistent with geomagnetic quiet conditions, and that is the standard value used in the GAIT model. To gauge the importance of this term, we varied the total Joule heating between 40 and 100 GW. Cases e and f in Table 3 show that the resulting change in the exospheric temperature is less than 5%, the biggest difference being at solar minimum when Joule heating is a larger fraction of the total heat input.

4.4. Heat Flux Boundary Condition

[57] In section 3.1 we described how differences in the heat flux boundary condition resulted in larger electron temperatures than calculated by R87 or R95. Through collisions, this also increases the neutral gas temperature. To examine this effect, we substituted the same 3×10^9 eV cm^{-2} s^{-1} heat flux used in R87 and R95 in place of our parameterized boundary condition. The sensitivity of the neutral gas exospheric temperature, shown in case g in Table 3, to this boundary condition is small, varying less than 2%. The electron temperature is much more sensitive; at the upper boundary T_e decreases 10% and 23% at solar minimum and maximum respectively.

4.5. Secondary Ionization by Photoelectrons

[58] Section 2.8 describes the approximate method used in the GAIT model to calculate secondary ionization by photoelectrons. R87 and R95 employed a fixed scale factor of 1.3 to approximate this effect. If this factor is adopted in the GAIT model, case h in Table 3, the exospheric temperature decreases by less than 3%, while the solar maximum TEC decreases about 8%.

4.6. Photoelectron Heating of Thermal Electrons

[59] The approximate photoelectron calculation is also used to specify the thermal electron volume heating rate. As noted in section 2.8, the peak heating rate calculated by GAIT is roughly 40% higher than parameterized values used in R87 and R95, which results in higher electron temperatures. Case i in Table 3 shows that the impact of using the parameterized heating rate is only 5 to 6% at solar maximum and less at solar minimum, when lower electron densities decrease the coupling between T_e and T_n.

[60] Of all the examples considered in Table 3, none changed the exospheric temperature by more than 13%, or the TEC by more than 23%. We therefore assert that the model is robust over the normal range of solar cycle variability, and the results determined primarily by changes in the solar irradiance. For this reason, we next examine more closely the choice of solar EUV irradiance model.

5. Model Response to EUV Representation

5.1. EUV Irradiance Models

[61] The results described so far have relied solely on the VUV irradiance model to represent the input solar flux [*Woods and Rottman*, 2002]. The VUV model specifies the solar irradiance at 1-nm resolution from 0 to 420 nm, although the GAIT model uses only those wavelengths between 3 and 360 nm. For wavelengths longward of 119 nm, the VUV reference spectrum and solar cycle variability are derived from measurements made by the Upper Atmosphere Research Satellite (UARS). At wavelengths less than 119 nm, the reference spectrum is based on a sounding rocket flight [*Woods et al.*, 1998], while the solar

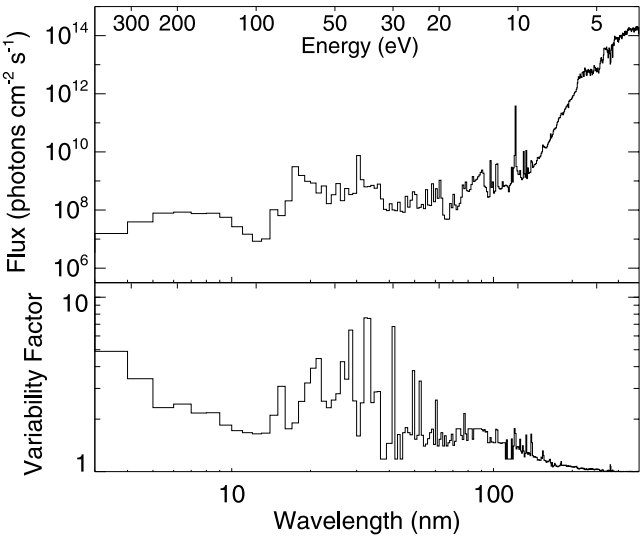

Figure 5. Standard solar input is based on the VUV model of *Woods and Rottman* [2002]. (top) VUV solar minimum reference spectrum (P = 70) and (bottom) multiplicative factor that must be applied to each wavelength bin in order to obtain a solar maximum spectrum (P = 230).

cycle variability is derived from four years of measurements made on the Atmospheric Explorer (AE-E) satellite during the ascending phase of solar cycle 21.

[62] In order to specify the irradiance at different phases of the solar cycle, we adopt a solar activity proxy. A number of different proxies are in use today, including the 10.7 cm solar radio flux (F10.7), its 81-day centered average ($\langle$F10.7$\rangle$), the Magnesium II core-to-wing ratio, and the composite Lyman-alpha index. The oldest proxies, F10.7 and $\langle$F10.7$\rangle$, are still widely used, however *Balan et al.* [1994a, 1994b] have argued that for high levels of solar activity the desired linear relationship between F10.7 and EUV irradiance breaks down. *Richards et al.* [1994] showed a similar breakdown, but found they could restore quasi-linearity over a wide range of solar activity by adopting a new proxy, P, defined as the average of the F10.7 and $\langle$F10.7$\rangle$ values,

$$P = (F10.7 + \langle F10.7 \rangle)/2 \quad (9)$$

We also adopt the P index, assuming it is linear with respect to the solar irradiance over the entire solar cycle.

[63] The VUV solar minimum and maximum reference spectra correspond to two 27-day periods centered on the dates 1996/108 and 1992/032 respectively. To employ the VUV model, we calculated the average P value centered on these dates and performed a simple linear fit. For a given level of solar activity, the photon flux in each wavelength bin is then determined by multiplying the solar minimum value by a factor that depends on the associated P index, seen in Figure 5. Figure 5 (top) shows the solar minimum (P = 70) photon flux, while Figure 5 (bottom) shows the multiplicative factor that must be applied to reach solar maximum (P = 230). This variability factor is simply the ratio of the solar maximum to minimum flux.

[64] As depicted in Figure 5, the shortest EUV wavelengths, which originate primarily in the solar corona, have the highest variability. The longer UV wavelengths originate lower in the solar atmosphere and have correspondingly lower variability. Extensive satellite measurements of these longer wavelengths have also established the absolute scale to the point that two different UV irradiance models [*Lean et al.*, 1997; *Woods and Rottman*, 2002] vary by less than 10% at all wavelengths (120–360 nm) over the course of the solar cycle, and in most cases by less than 5%. By contrast, models of the EUV irradiance differ significantly in both absolute scale and solar cycle variability [*Lean et al.*, 2003]. To gauge the importance of these differences we will consider three other EUV irradiance representations.

[65] The widely used EUVAC model was developed by *Richards et al.* [1994]. The model's absolute scale is based on the F74113 reference spectrum [*Torr et al.*, 1979], and the solar cycle variation is specified by AE-E results. EUVAC doubles the F74113 photon fluxes below 25 nm in order to improve agreement between observed and modeled photoelectron spectra [*Richards and Torr*, 1984]. The model uses the P index as its solar activity proxy, and, as we have done with the VUV model, assumes a linear variation with P across the solar cycle.

[66] The Solar2000 (S2000) model is the most recent in a series of iterations by *Tobiska et al.* [2000]. S2000 incorporates measurements made by multiple satellite and rocket measurements, including the AE-E observations, to specify both the reference spectrum and solar variability. The model is updated regularly to include the latest measurements, and the work here uses version 2.21. The daily F10.7 and a composite Lyman-α index are used as the principal solar activity proxies.

[67] Whereas the previous three models are purely empirical, *Warren et al.* [2001] have used a different approach to create the NRLEUV model. Measurements of the EUV

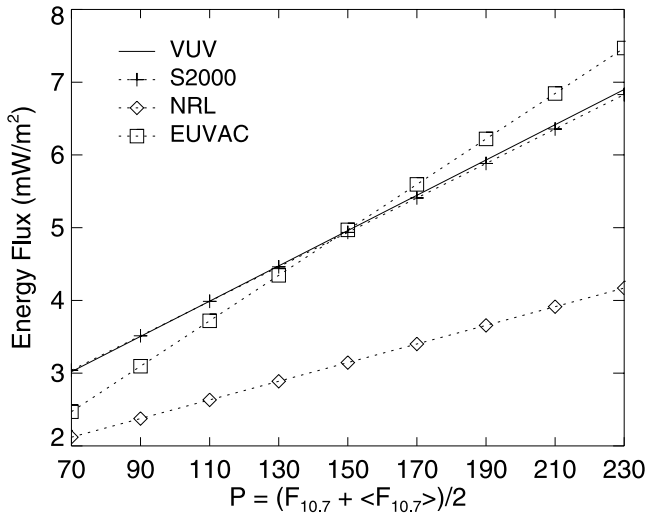

Figure 6. A comparison of the integrated EUV energy flux (3–105 nm) as a function of solar activity, calculated using four different irradiance models. The solid line corresponds to the standard input, the VUV model [*Woods and Rottman*, 2002], while the dotted lines with crosses, diamonds, and squares correspond to the Solar2000 version 2.21 [*Tobiska et al.*, 2000], NRLEUV [*Warren et al.*, 2001], and EUVAC [*Richards et al.*, 1994] models, respectively.

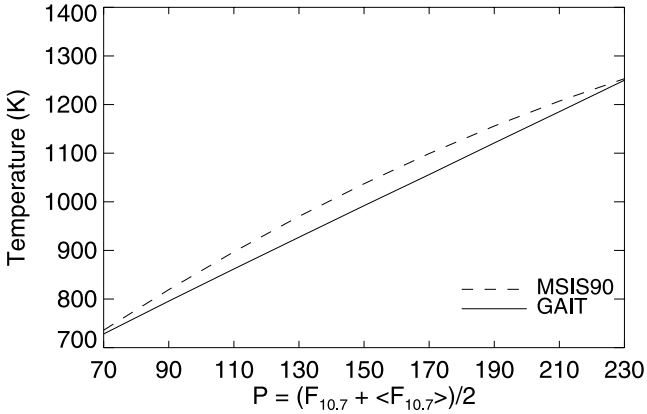

Figure 7. Model calculations of the global mean exospheric temperature as a function of the solar cycle, assuming quiet geomagnetic conditions (Ap = 4). The solid line corresponds to the GAIT model results, and the dashed line corresponds to the MSIS-90 empirical model.

emission from specific solar structures (e.g., quiet Sun, active regions, network, and coronal holes) and the fractional solar disk coverage of these features is used to compute the EUV irradiance. The solar minimum irradiance, which establishes the absolute scale, is calculated by integrating the "quiet Sun" emission over the entire disk. At other times, the irradiance is adjusted by including the presence of additional features. A parameterized version uses F10.7, ⟨F10.7⟩, and the Magnesium II core-to-wing ratio as proxies to solar activity.

[68] Just as described previously for the VUV model, we parameterized the output from these other irradiance models with the P index. To do this, we averaged two months of output from each model to create representative minimum (September 1986) and maximum (November 1989) spectra; linear interpolation is then performed using the average P index for both months, 70 and 221 respectively. The EUVAC model required no parameterization since it uses the P index intrinsically.

[69] *Lean et al.* [2003] conducted an extensive comparison between NRLEUV, EUVAC, and an earlier version of S2000 (v1.15). One of the main conclusions they reached was that the NRLEUV model predicted overall lower irradiances and a smaller solar cycle variability in the EUV than the other empirical models. A comparison of the integrated EUV energy flux predicted by each of the four irradiance models is given in Figure 6. Since each irradiance model has been fit linearly between solar minimum and maximum, the energy flux varies linearly with P as well. As expected from the *Lean et al.* [2003] results, the NRLEUV model returns the lowest absolute energy flux, 2.12 mW/m^2 at solar minimum, as well as the lowest solar cycle variation, a factor of 1.97. The EUVAC model predicts the largest variation, a factor of 3.02, starting from 2.47 mW/m^2 at solar minimum. The total energy flux for the VUV and S2000 models are nearly identical, 3.02 and 3.04 mW/m^2 at solar minimum and 6.90 and 6.83 mW/m^2 at maximum, although we will see that spectral differences between the two are reflected in the results.

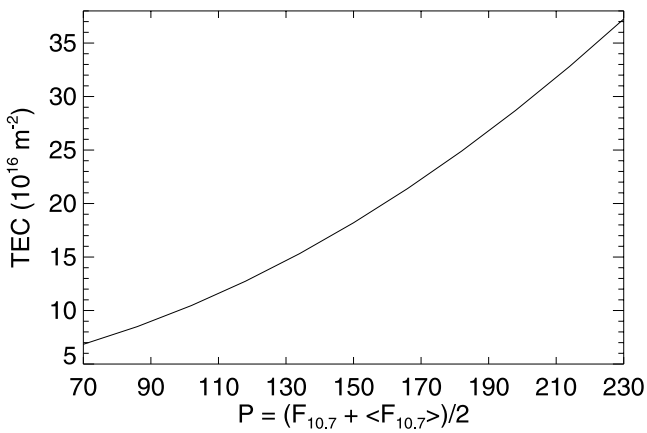

Figure 8. Model calculations of the total electron content as a function of the solar cycle, assuming quiet geomagnetic conditions (Ap = 4).

5.2. Solar Cycle Response

[70] Making use of the proxy, P, we examine the response of the thermosphere and ionosphere across a range of solar activity. The exospheric temperature and TEC are again chosen as scalar indicators for the overall state of the thermosphere and ionosphere respectively. Figure 7 shows the calculated global mean exospheric temperature ranging from solar minimum, P = 70, to solar maximum, P = 230, while Figure 8 details the TEC response. We assumed quiet geomagnetic conditions (Ap = 4), keeping the global Joule heating input fixed at 70 GW, and initially used only the VUV irradiance model for solar input.

[71] Figure 7 also includes MSIS-90 global average exospheric temperatures. The two models agree best at solar minimum and maximum, because these are the points used to tune the GAIT model. In between, the MSIS-90

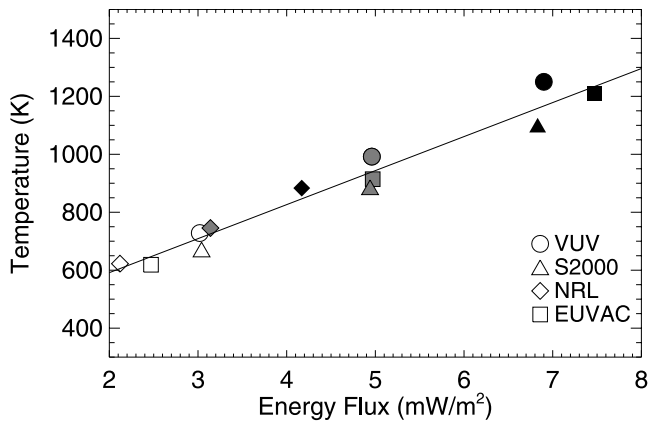

Figure 9. Modeled global mean exospheric temperatures as a function of the EUV energy flux (3–105 nm), calculated using four different irradiance models. The circles, triangles, diamonds, and squares correspond to the VUV [*Woods and Rottman*, 2002], Solar2000 version 2.21 [*Tobiska et al.*, 2000], NRLEUV [*Warren et al.*, 2001], and EUVAC [*Richards et al.*, 1994] models respectively. Open symbols represent solar minimum conditions (P = 70), solid symbols solar maximum conditions (P = 230), and shaded symbols moderate solar conditions (P = 150). The solid line indicates a least squares fit to the results.

temperatures are higher, the greatest difference being 45 K or 4.6% at P = 150. The exospheric temperatures calculated with the GAIT model show a remarkable linearity across a range of solar activity. Since the energy flux scales linearly with P (Figure 6), this implies that the neutral gas temperature responds linearly to the input energy over the normal solar cycle range. On the other hand, the MSIS-90 exospheric temperatures show a knee at roughly P = 150. Assuming the physical model is correct, and the thermosphere does respond linearly to the energy input, the MSIS-90 results imply the solar irradiance is not linear with P, in agreement with the work of *Balan et al.* [1994a, 1994b]. This suggests that to better match the nonlinear MSIS-90 response we should adopt a nonlinear irradiance model.

[72] TEC depends, of course, on both the peak electron density (N_mF_2) as well as the slab thickness. N_mF_2 is found to increase nearly linearly over the course of the solar cycle. In pressure coordinates the slab thickness is approximately constant [*Rishbeth and Edwards*, 1989], which means it too should increase roughly linearly in absolute height, given a linear increase in neutral temperature. Convolving these two components results in a nonlinear, approximately quadratic increase to TEC. The actual variation of TEC deviates from this description because of the effect of T_e and T_i. As shown in Figure 8, the global mean electron content increases from 6.8 TEC units at solar minimum to 37.5 units at solar maximum (1 TEC unit = 10^{16} electrons/m^2).

[73] To contrast the effect of different EUV models, the GAIT model was run for low, moderate, and high solar activity using each of the four irradiance representations as input, while keeping the other parameters fixed. The resulting exospheric temperatures are plotted in Figure 9 as a function of the integrated EUV energy flux (3–105 nm). In Figure 9, each of the four irradiance models are identified by a different symbol: VUV (circle), S2000 (triangle), NRLEUV (diamond), and EUVAC (square). Each symbol is also color coded according to the solar activity level: open (low, P = 70), shaded (moderate, P = 150), and solid (high, P = 230). The solid line represents a linear least squares fit to the results.

[74] The modeled exospheric temperature responds linearly to each of the four irradiance representations, although the slope varies slightly because of the spectral differences between them. For example, even though the VUV and S2000 models predict essentially the same total energy flux, the S2000 exospheric temperatures are 8% smaller at solar minimum and 12% smaller at maximum. Although for clarity they are not shown in Figure 9, temperatures calculated using the early EUV representation of R87 also fall within 5% of the solid line. A similar figure (not shown) contrasting the TEC response to the four EUV models also produces a cluster around a best fit curve; although there is slightly more spread in the data.

[75] The NRLEUV results are particularly striking, and the impact of its smaller dynamic range is readily apparent. As Figures 6 and 9 illustrate, the total energy input predicted by NRLEUV for high solar activity (P = 230) is less than that predicted by the other three models for moderate activity (P = 150). The exospheric temperatures are correspondingly low; using NRLEUV the model returns an unphysical solar maximum temperature of 883 K, 30% lower than the MSIS-90 model.

[76] Another conclusion to be drawn from Figure 9 is that key reaction rates and inputs must be tuned to a specific irradiance representation. The GAIT model has been tuned to the VUV model; as a consequence none of the other irradiance models result in exospheric temperatures within 10% of MSIS-90. By simply adjusting some of the key parameters as listed in Table 3, exospheric temperatures calculated using both the S2000 and EUVAC models can be easily brought within 2% of the empirical model at both solar minimum and maximum. However, we could find no combination of reasonable adjustments sufficient to bring the NRLEUV output into agreement. Even after modifying all of the reaction rates and inputs listed in Table 3 to give the highest temperatures, the NRLEUV solar maximum temperature only reached 1148 K, still 8% less than the MSIS-90 value. Furthermore, these changes increased the solar minimum temperature to 802 K, 9% larger than the empirical value. Barring significant changes to the accepted reaction rates or new nonlinear heat sources, the dynamic range of the NRLEUV model is apparently not large enough to support the observed solar cycle temperature variation.

5.3. Wavelength Sensitivity

[77] *Roble* [1987] performed a wavelength-dependent sensitivity study by systematically zeroing the photon flux in each of the model's EUV wavelength bins and computing the change induced in the exospheric temperature. The bins were rank ordered according to their relative importance, for both solar minimum and maximum. He found the order depended slightly on the solar cycle, although the top three bins remained the same. Per Figure 5, the solar cycle variability factor is wavelength-dependent; hence the results of a sensitivity study involving irradiance will also be inherently a function of solar activity. Recognizing this, we conducted a study similar to Roble's, centered at average solar conditions, P = 150.

[78] Akin to the *Roble* [1987] work, we systematically zeroed the photon flux in 5-nm wide wavelength intervals. The output from each run was then compared to the unaltered reference run. Figure 10 details the relative fractional change of key parameters as a function of the EUV wavelength. The three panels in Figure 10 correspond to the changes in the neutral gas exospheric temperature, peak F region ionospheric electron density (N_mF_2), and peak E region electron density (N_mE).

[79] From Figure 10 (top), we see the largest temperature sensitivity occurs between 15 and 35 nm, particularly in two bands: 15–20 nm and 30–35 nm. Employing 1-nm resolution, we find the single most important wavelength interval is 30–31 nm, which includes the strong He II line at 30.37 nm. This matches the earlier *Roble* [1987] results, which found the 30.37 nm line to provide the most important contribution at both solar minimum and maximum. *Roble*'s [1987] top three contributors also included 85–90 nm and 15–20 nm, in that order. Although zeroing the 85–90 nm bin produces an approximately 5% change in temperature, it only ranks fifth in overall importance on the basis of the GAIT model results. The model used by *Roble* [1987] relied on parameterizations and scale factors to account for photoelectrons, which were not directly affected by eliminating the high-energy photons; this effectively increases the relative importance of long-wavelength

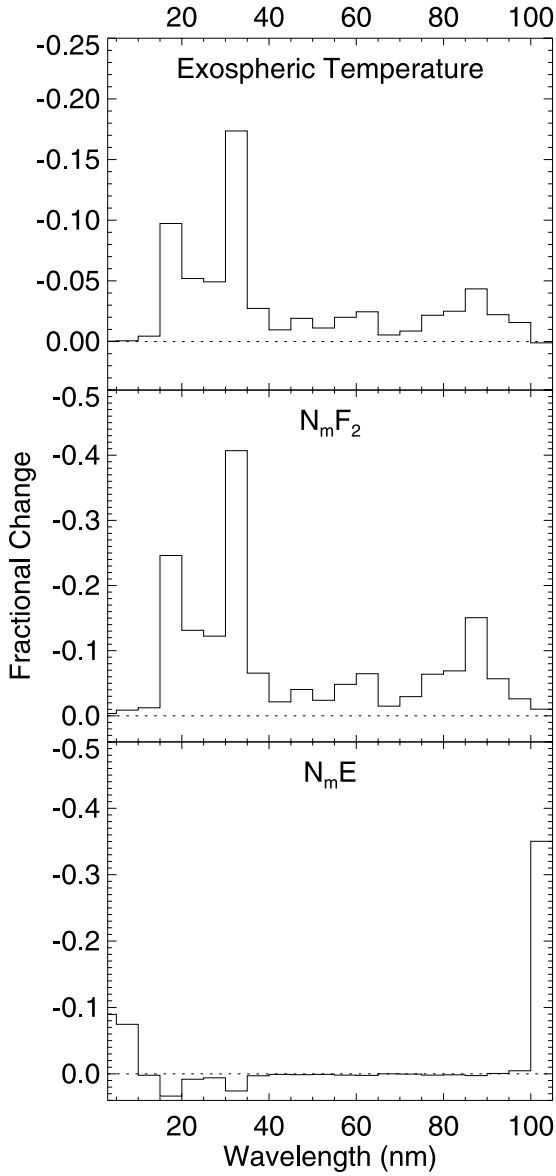

Figure 10. Wavelength sensitivity of the (top) neutral exospheric temperature, (middle) N_mF_2 (middle), and (bottom) N_mE. The fractional change of each parameter from a reference value is computed after zeroing the photon flux in the corresponding 5-nm wide bin.

photons. On the other hand, the GAIT model, which includes a self-consistent photoelectron calculation, responds more strongly to the flux of short-wavelength photons. Another important distinction between the GAIT and *Roble* [1987] results is the EUV model used to represent the irradiance. More recent measurements of the EUV have increased the flux of short-wavelength photons relative to the irradiance models available at the time of Roble's work. The GAIT model incorporates these new values, further increasing the importance of the short-wavelength bins.

[80] Another way to consider the wavelength-dependent temperature sensitivity is via the relative energy flux contained within each interval. The exospheric temperatures plotted in Figure 9 respond nearly linearly to the input EUV energy flux. On the basis of Figure 5 we find the largest contribution to the total EUV energy flux occurs between 15 and 35 nm. It is therefore not surprising that the largest temperature effect occurs in these same wavelength bins. If the fractional EUV energy content of each bin were superimposed upon the temperature sensitivity shown in Figure 10 (top), the two curves would be very similar. In fact, between 35 and 90 nm, the two curves are nearly identical. At longer and shorter wavelengths, the fractional energy content is greater than the relative temperature response; however, the trends are generally the same. For example, using the VUV model, the five largest EUV energy contributions come from bins in the range 15–35 nm and 85–90 nm, which correspond to the top five bins for temperature sensitivity, in the same order. The wavelength sensitivity of the exospheric temperature is therefore determined primarily by the energy content of the individual bins.

[81] Figure 10 (middle) displays the relative change observed in N_mF_2 after zeroing the respective wavelength intervals. It is apparent from Figure 10 that the N_mF_2 sensitivity is very similar to the neutral temperature response. Sorting the bins by their relative importance produces nearly the same order in both cases. Ionization at the F_2 peak implies energy deposition, so it is not surprising the two responses correlate well. While the relative importance of the bins is roughly the same, the fractional change is not. In nearly every case, the change is larger for N_mF_2 than the temperature. For example, N_mF_2 decreases by 40% when the 30–35 nm bin is zeroed, whereas the exospheric temperature only decreases by 17%. At 85–90 nm, the decreases are 15% and 4% respectively. This highlights the fact that N_mF_2 is determined not only by the incident photon flux, but also the underlying thermosphere, which itself is affected by the photon flux. This result underscores the coupled nature of the ionosphere and thermosphere, and is considered further in the companion paper.

[82] Figure 10 (bottom) depicts the change of N_mE to the same sensitivity analysis. While the variation of temperature and N_mF_2 correlated strongly to the input energy flux, N_mE responds almost exclusively to the long- and short-wavelength wings of the EUV. The largest relative contribution comes from the 100–105 nm bin; zeroing the flux in this bin decreases N_mE by 35%. If the analysis is performed using 1-nm wide bins, we find nearly all of this sensitivity is due to the range 102–103 nm, which includes the H I line at 102.57 nm. The remainder of the contribution arises from photons between 3 and 10 nm. Only those photons not readily absorbed in the F region are available to penetrate to the E region, thus sensitivity to the wings of the EUV photons merely reflects the absorption cross sections for N_2, O_2, and O. In the case of the H I line at 102.57 nm, the N_2 and O cross sections are zero, allowing the photons to pass through the upper atmosphere. The O_2 cross section is also relatively small at this wavelength; however, the photon flux is large enough to make this the dominant contributor to N_mE.

[83] In two wavelength bands, 15–20 nm and 30–35 nm, zeroing the photon flux actually increases N_mE. While initially counterintuitive, recall these same two bands contribute the most to the exospheric temperature. By eliminating the flux in these bands, the neutral gas temperature drops and the atmosphere contracts. With less intervening atmosphere, more photons at other wavelengths penetrate to the lower E region.

[84] Although not shown in Figure 10, we also considered the wavelength sensitivity of N_mF_1. In some cases it was not possible to identify a local F_1 layer maximum in the electron density profile. For the purpose of this analysis we calculated N_mF_1 on the basis of the electron density at the height where the sum of the molecular ions is a maximum. This approach identifies the correct value when a local maximum exists at the F_1 layer, and provides a representative number when it does not.

[85] The N_mF_1 sensitivity results are not shown because they are nearly identical to those of the exospheric temperature. Across the range 3–80 nm the relative change induced in N_mF_1 is the same as that in the temperature, to within less than 1% and in most cases to within less than 0.5%. Between 80 and 100 nm, N_mF_1 responds slightly less than the temperature to the removal of photons, but the relative changes are still within 4% of each other. All of this indicates the N_mF_1 response is strongly linked to energy deposition and the resulting temperature, even more so than was the case for N_mF_2.

6. Conclusion

[86] We have described a new model representing the coupled global average ionosphere and thermosphere (GAIT). Our development effort focused on making the model independent of a specific solar irradiance representation, and therefore able to accurately respond to a wide range of irradiance inputs. Results from the GAIT model were compared to the empirical MSIS-90 model as well as earlier global average models and shown to be in reasonable agreement with both.

[87] Large uncertainties remain in several key reaction rates, which, in turn, directly influence the thermospheric energy balance. We examined the sensitivity of the GAIT model to these uncertainties and found that even the most significant resulted in less than a 13% change to the exospheric temperature. Given that the ''observed'' exospheric temperature varies by more than 70% over the course of the solar cycle, none of the known uncertainties drives the final result.

[88] In addition to the standard VUV irradiance model, we considered the sensitivity to three alternate EUV representations: the EUVAC, S2000, and NRLEUV models. Consistent with the results of *Lean et al.* [2003], the total EUV energy flux predicted by each of the four models differed markedly. The NRLEUV model predicted the lowest total energy flux; it also had the smallest dynamic range. However, regardless of which irradiance model was used, the modeled exospheric temperature scaled linearly with the total EUV energy input. By varying just one or two of the uncertain parameters described in Table 3, we were able to bring the VUV, EUVAC, and S2000 models to within 2% of the MSIS-90 results. However, no combination brought the NRLEUV temperatures within 9% of MSIS-90. We concluded that the dynamic range of the NRLEUV model is not large enough to support the observed variation in the neutral gas temperature.

[89] An analysis of wavelength sensitivity showed that the exospheric temperature, N_mF_2, and N_mF_1 all responded similarly, driven primarily by the energy flux contained within each EUV band. In all three cases, removal of photons in the range 15–35 nm caused the most significant changes, precisely the range containing the greatest energy flux. Most important of all was the contribution from the He II line at 30.37 nm. Elimination of photons in the 30–35 nm bin caused a 17% decrease in N_mF_1 and temperature, and a 40% decrease in N_mF_2. The sensitivity of N_mF_1 and temperature were nearly identical at all wavelengths, while the N_mF_2 response was generally larger. By contrast, the response of N_mE reflected the requirement that photons must be able to penetrate to low enough altitudes to have an impact. Photons in the range 3–10 nm and the H I line at 102.57 nm produced the strongest response in N_mE, indicative of the low absorption cross sections at these wavelengths.

[90] **Acknowledgments.** This research was supported by NASA grant NAG5-8227 and NSF grant ATM-0000171 to Utah State University. Christopher Smithtro was supported by the Air Force Institute of Technology. The authors would like to thank Judith Lean, Scott Bailey, Tom Woods, Ken Minschwaner, Phil Richards, and J. B. Nee for their helpful contributions. Solar2000 irradiances are provided courtesy of W. Kent Tobiska and SpaceWx.com. The EUV irradiance models have been developed with funding from NASA and ONR. The views expressed in this article are those of the authors and do not necessarily reflect the official policy or position of the Air Force, the Department of Defense, or the U.S. Government.

[91] Arthur Richmond thanks Pierre-Louis Blelly and Dirk Lummerzheim for their assistance in evaluating this manuscript.

References

Allen, M., J. I. Lunine, and Y. L. Yung (1984), The vertical distribution of ozone in the mesosphere and lower thermosphere, *J. Geophys. Res.*, *89*(D3), 4841–4872.

Balan, N., G. J. Bailey, B. Jenkins, P. B. Rao, and R. J. Moffett (1994a), Variations of ionospheric ionization and related solar fluxes during an intense solar cycle, *J. Geophys. Res.*, *99*(A2), 2243–2253.

Balan, N., G. J. Bailey, and R. J. Moffett (1994b), Modeling studies of ionospheric variations during an intense solar cycle, *J. Geophys. Res.*, *99*(A9), 17,467–17,475.

Bates, D. R. (1951), The temperature of the upper atmosphere, *Proc. Phys. Soc. London, Sect. B*, *64*, 805–821.

Chapman, S., and T. G. Cowling (1952), *The Mathematical Theory of Non-Uniform Gases*, 423 pp., Cambridge Univ. Press, New York.

Colegrove, F. D., F. S. Johnson, and W. B. Hanson (1966), Atmospheric composition in the lower thermosphere, *J. Geophys. Res.*, *71*(9), 2227–2236.

Craig, R. A., and J. C. Gille (1969), Cooling of the thermosphere by atomic oxygen, *J. Atmos. Sci.*, *26*, 205–209.

Duff, J., and R. D. Sharma (1997), Quasiclassical trajectory study of the relaxation of vibrationally excited NO by collisions with O atoms, *J. Chem. Soc. Faraday Trans.*, *93*, 2645–2649.

Durrance, S. T., and G. E. Thomas (1979), The 63 μm radiation field in the Earth's thermosphere and its influence on the atomic hydrogen temperature, *Planet. Space Sci.*, *27*, 795–800.

Fell, C., J. I. Steinfield, and S. Miller (1990), Quenching of $N(^2D)$ by $O(^3P)$, *J. Chem. Phys.*, *92*, 4768–4777.

Fennelly, J. A., and D. G. Torr (1992), Photoionization and photoabsorption cross sections of O, N_2, O_2, and N for aeronomic calculations, *At. Data Nucl. Data Tables*, *51*, 321–363.

Fomichev, V. I., J. P. Blanchet, and D. S. Turner (1998), Matrix parameterization of the 15 μm CO_2 band cooling in the middle and upper atmosphere for variable CO_2 concentration, *J. Geophys. Res.*, *103*(D10), 11,505–11,528.

Glenar, D. A., E. Bleuler, and J. S. Nisbet (1978), The energy balance of the nighttime thermosphere, *J. Geophys. Res.*, *83*(A12), 5550–5562.

Gordiets, B. F., Y. N. Kulikov, M. N. Markov, and M. Y. Marov (1982), Numerical modeling of the thermospheric heat budget, *J. Geophys. Res.*, *87*(A6), 4504–4514.

Green, A. E. S., and R. S. Stolarski (1972), Analytic models of electron impact excitation cross sections, *J. Atmos. Terr. Phys.*, *34*, 1703–1717.

Grossmann, K. U., and D. Offermann (1978), Atomic oxygen emission at 63 μm as a cooling mechanism in the thermosphere and ionosphere, *Nature*, *276*, 594–595.

Grossmann, K. U., and K. Vollmann (1997), Thermal infrared measurements in the middle and upper atmosphere, *Adv. Space Res.*, *19*, 631–638.

Hedin, A. E. (1991), Extension of the MSIS thermosphere model into the middle and lower atmosphere, *J. Geophys. Res.*, *96*(A2), 1159–1172.

Hinteregger, H. E., K. Fukui, and B. R. Gilson (1981), Observational, reference and model data on solar EUV, from measurements on AE-E, *Geophys. Res. Lett.*, *8*(11), 1147–1150.

Jackman, C. H., R. H. Garvey, and A. E. S. Green (1977), Electron impact on atmospheric gases: 1. Updated cross sections, *J. Geophys. Res.*, *82*(32), 5081–5090.

Jet Propulsion Laboratory, (2003), Chemical kinetics and photochemical data for use in atmospheric studies, evaluation 14, *JPL Publ. 02-25*, Pasadena, Calif.

Johnson, F. S., and B. Gottlieb (1970), Eddy mixing and circulation at ionospheric levels, *Planet. Space Sci.*, *18*, 1707–1718.

Kockarts, G. (1980), Nitric oxide cooling in the terrestrial thermosphere, *Geophys. Res. Lett.*, *7*(2), 137–140.

Kockarts, G., and W. Peetermans (1970), Atomic oxygen infrared emission in the Earth's upper atmosphere, *Planet. Space Sci.*, *18*, 271–285.

Lean, J. L., G. J. Rottman, H. L. Kyle, T. N. Woods, J. R. Hickey, and L. C. Puga (1997), Detection and parameterization of variations in the solar mid and near ultraviolet radiation (200 to 400 nm), *J. Geophys. Res.*, *102*, 29,939–29,956.

Lean, J. L., H. P. Warren, J. T. Mariska, and J. Bishop (2003), A new model of solar EUV irradiance variability: 2. Comparisons with empirical models and observations and implications for space weather, *J. Geophys. Res.*, *108*(A2), 1059, doi:10.1029/2001JA009238.

Lee, P. C., and J. B. Nee (2000), Detection of $O(^1D)$ produced in the photodissociation of O_2. I. Identification of the $^3\Sigma_u$ and $^3\Pi_u$ Rydberg states in 113–130 nm, *J. Chem. Phys.*, *112*(4), 1763–1768.

Lettau, H. (1951), Diffusion in the upper atmosphere, in *Compendium of Meteorology*, edited by T. Malone, pp. 320–335, Am. Meteorol. Soc., New York.

Minschwaner, K., and D. E. Siskind (1993), A new calculation of nitric oxide photolysis in the stratosphere, mesosphere, and lower thermosphere, *J. Geophys. Res.*, *98*(D11), 20,401–20,412.

Minschwaner, K., R. J. Salawitch, and M. B. McElroy (1993), Absorption of solar radiation by O_2: Implications for O_3 and lifetimes of N_2O, $CFCl_3$, and CF_2Cl_2, *J. Geophys. Res.*, *98*(D6), 10,543–10,561.

Mlynczak, M. G., and S. Solomon (1993), A detailed evaluation of the heating efficiency in the middle atmosphere, *J. Geophys. Res.*, *98*(D6), 10,517–10,541.

Nee, J. B., and P. C. Lee (1997), Detection of $O(^1D)$ produced in the photodissociation of O_2 in the Schumann-Runge continuum, *J. Phys. Chem. A*, *101*, 6653–6657.

Nicolet, M. (1985), Aeronomical aspects of mesospheric photodissociation: Processes resulting from the solar H Lyman-alpha line, *Planet. Space Sci.*, *33*(1), 69–80.

Pollock, D. S., G. B. I. Scott, and L. F. Phillips (1993), Rate constant for the quenching of $CO_2(010)$ by atomic oxygen, *Geophys. Res. Lett.*, *20*(8), 727–729.

Rees, M. H. (1989), *Physics and Chemistry of the Upper Atmosphere*, 289 pp., Cambridge Univ. Press, New York.

Rees, M. H., and R. G. Roble (1975), Observations and theory of the formation of stable auroral red arcs, *Rev. Geophys.*, *13*(1), 201–242.

Richards, P. G., and D. G. Torr (1983), A simple theoretical model for calculating and parameterizing the ionospheric photoelectron flux, *J. Geophys. Res.*, *88*(A3), 2155–2162.

Richards, P. G., and D. G. Torr (1984), An investigation of the consistency of the ionospheric measurements of the photoelectron flux and solar EUV flux, *J. Geophys. Res.*, *89*(A7), 5625–5635.

Richards, P. G., and D. G. Torr (1988), Ratios of photoelectron to EUV ionization rates for aeronomic studies, *J. Geophys. Res.*, *93*(A5), 4060–4066.

Richards, P. G., J. A. Fennelly, and D. G. Torr (1994), EUVAC: A solar EUV flux model for aeronomic calculations, *J. Geophys. Res.*, *99*(A5), 8981–8992.

Rishbeth, H., and R. Edwards (1989), The isobaric F_2-layer, *J. Atmos. Terr. Phys.*, *51*, 321–338.

Roble, R. G. (1987), Solar cycle variation of the global mean structure of the thermosphere, paper presented at Workshop on Solar Radiative Output Variation, Natl. Cent. for Atmos. Res., Boulder, Colo.

Roble, R. G. (1995), Energetics of the mesosphere and thermosphere, in *The Upper Mesosphere and Lower Thermosphere: A Review of Experiment and Theory*, *Geophys. Monogr. Ser.*, vol. 87, edited by R. M. Johnson and T. L. Killeen, pp. 1–21, AGU, Washington, D. C.

Roble, R. G., and B. A. Emery (1983), On the global mean temperature of the thermosphere, *Planet. Space Sci.*, *31*(6), 597–614.

Roble, R. G., E. C. Ridley, and R. E. Dickinson (1987), On the global mean structure of the thermosphere, *J. Geophys. Res.*, *92*(A8), 8745–8758.

Schunk, R. W. (1988), A mathematical model of the middle and high latitude ionosphere, *Pure Appl. Geophys.*, *127*, 255–303.

Schunk, R. W., and A. F. Nagy (2000), *Ionospheres: Physics, Plasma Physics, and Chemistry*, Cambridge Univ. Press, New York.

Sharma, R. D., and P. P. Wintersteiner (1990), Role of carbon dioxide in cooling planetary thermospheres, *Geophys. Res. Lett.*, *17*(12), 2201–2204.

Sharma, R. D., B. Zygelman, F. von Esse, and A. Dalgarno (1994), On the relationship between the population of the fine structure levels of the ground electronic state of atomic oxygen and the translational temperature, *Geophys. Res. Lett.*, *21*(16), 1731–1734.

Shemansky, D. E. (1972), CO_2 extinction coefficient 1700–3000 Å, *J. Chem. Phys.*, *56*(4), 1582–1587.

Shved, G. M., L. E. Khvorostovskaya, I. Y. Potekhin, A. I. Demyanikov, A. A. Kutepov, and V. I. Fomichev (1991), Measurement of the quenching rate constant for collisions $CO_2(010)$-O: The importance of the rate constant magnitude for the thermal regime and radiation of the lower thermosphere, *Atmos. Oceanic Phys.*, *27*, 431–437.

Smith, F. L., III, and C. Smith (1972), Numerical evaluation of Chapman's grazing incidence integral ch (X,χ), *J. Geophys. Res.*, *77*(19), 3592–3597.

Solomon, S. C., P. B. Hays, and V. J. Abreu (1988), The auroral 6300 Å emission: Observations and modeling, *J. Geophys. Res.*, *93*(A9), 9867–9882.

Strobel, D. F. (1978), Parameterization of the atmospheric heating rate from 15 to 120 km due to O_2 and O_3 absorption of solar radiation, *J. Geophys. Res.*, *83*(C12), 6225–6230.

Swartz, W. E., and J. S. Nisbet (1972), Revised calculations of F region ambient electron heating by photoelectrons, *J. Geophys. Res.*, *77*(31), 6259–6261.

Titheridge, J. E. (1998), Temperatures in the upper ionosphere and plasmasphere, *J. Geophys. Res.*, *103*(A2), 2261–2277.

Tobiska, W. K., T. Woods, F. Eparvier, R. Viereck, L. Floyd, D. Bouwer, G. Rottman, and O. R. White (2000), The SOLAR2000 empirical solar irradiance model and forecast tool, *J. Atmos. Sol. Terr. Phys.*, *62*, 1233–1250.

Torr, M. R., and D. G. Torr (1980), Solar flux variability in the Schumann-Runge continuum as a function of solar cycle 21, *J. Geophys. Res.*, *85*(A11), 6063–6068.

Torr, M. R., and D. G. Torr (1985), Ionization frequencies for solar cycle 21: Revised, *J. Geophys. Res.*, *90*(A7), 6675–6678.

Torr, M. R., D. G. Torr, and R. A. Ong (1979), Ionization frequencies for major thermospheric constituents as a function of solar cycle 21, *Geophys. Res. Lett.*, *6*(10), 771–774.

Trinks, H., and K. H. Fricke (1978), Carbon dioxide concentrations in the lower thermosphere, *J. Geophys. Res.*, *83*(A8), 3883–3886.

Warren, H. P., J. T. Mariska, and J. Lean (2001), A new model of solar EUV irradiance variability: 1. Model formulation, *J. Geophys. Res.*, *106*(A8), 15,745–15,757.

Wennberg, P. O., J. G. Anderson, and D. K. Weisenstein (1994), Kinetics of reactions of ground state nitrogen atoms ($^4S_{3/2}$) with NO and NO_2, *J. Geophys. Res.*, *99*(D9), 18,839–18,846.

Woods, T. N., and G. J. Rottman (2002), Solar ultraviolet variability over time periods of aeronomic interest, in *Atmospheres in the Solar System: Comparative Aeronomy*, *Geophys. Monogr. Ser.*, vol. 130, edited by M. Mendillo et al., pp. 221–233, AGU, Washington, D. C.

Woods, T. N., G. J. Rottman, S. M. Bailey, S. C. Solomon, and J. Worden (1998), Solar extreme ultraviolet irradiance measurements during solar cycle 22, *Sol. Phys.*, *177*, 133–146.

Yoshino, K., J. R. Esmond, Y. Sun, W. H. Parkinson, K. Ito, and T. Matsui (1996), Absorption cross section measurements of carbon dioxide in the wavelength region 118.7–175.5 nm and the temperature dependence, *J. Quant. Spectrosc. Radiat. Trans.*, *55*(1), 53–60.

C. G. Smithtro, Air Force Institute of Technology, Wright-Patterson AFB, OH 45433-7765, USA. (christopher.smithtro@afit.edu)

J. J. Sojka, Center for Atmospheric and Space Sciences, Utah State University, Logan, UT 84322-4405, USA.